Approaching neutron-rich nuclei toward the *r*-process path in peripheral heavy-ion collisions at 15 MeV/nucleon

G. A. Souliotis,[1,2,*] M. Veselsky,[3] S. Galanopoulos,[2,†] M. Jandel,[2,‡] Z. Kohley,[2,4,§] L. W. May,[2,4] D. V. Shetty,[2,‖]
B. C. Stein,[2,4] and S. J. Yennello[2,4]

[1]*Laboratory of Physical Chemistry, Department of Chemistry, National and
Kapodistrian University of Athens and Hellenic Institute of Nuclear Physics, Athens GR-15771, Greece*
[2]*Cyclotron Institute, Texas A&M University, College Station, Texas 77843, USA*
[3]*Institute of Physics, Slovak Academy of Sciences, Bratislava SK-84511, Slovakia*
[4]*Chemistry Department, Texas A&M University, College Station, Texas 77843, USA*

The production cross sections of projectilelike fragments from the interaction of 15 MeV/nucleon ^{86}Kr with ^{64}Ni and ^{58}Ni and with ^{124}Sn and ^{112}Sn were measured using a magnetic separator with emphasis on the neutron-rich isotopes. Neutron pickup isotopes (with up to six neutrons picked up from the target) were observed with large cross sections. Calculations involving the the deep-inelastic transfer model as well as the microscopic constrained molecular dynamics model (CoMD) for the primary interaction stage coupled to the statistical deexcitation code GEMINI were used to describe the gross properties of the product distributions. The present results were also compared with our previous data of the same reactions at 25 MeV/nucleon. The data at 15 MeV/nucleon show enhanced production of neutron-rich isotopes very close to the projectile, relative to the corresponding data at 25 MeV/nucleon. This enhancement in the cross sections is possibly associated with very peripheral collisions and longer interaction times of the neutron-rich ^{86}Kr projectile with the neutron-rich targets. The large cross sections of such reactions well above the Coulomb barrier, but below the Fermi energy, involving peripheral nucleon exchange, suggest that both the N/Z of the projectile and the N/Z of the target may properly be exploited in the production of neutron-rich rare isotopes. These reactions offer a novel and attractive route to access extremely neutron-rich rare isotopes toward the the astrophysical *r*-process path and, possibly, the neutron drip-line.

PACS number(s): 25.70.Hi, 25.70.Lm

I. INTRODUCTION

Access and study of new regions of the nuclear landscape toward the neutron drip-line is currently one of the major efforts in nuclear physics research. Investigation of very neutron-rich nuclei offers the possibility to follow the evolution of nuclear structure with increasing neutron-to-proton ratio (N/Z) [1] and to elucidate important nucleosynthesis processes [2], most notably the rapid neutron-capture process (*r*-process) [3,4]. Furthermore, reactions induced by neutron-rich nuclei can provide information on the isospin dependence of the effective nucleon-nucleon interaction and, thus, shed light on the equation of state [5–8] of asymmetric nuclear matter, which is an important ingredient of the physics of supernovas [9] and neutron stars [10,11].

For the aforementioned reasons, the efficient production of very neutron-rich nuclides is a central issue in current and future rare isotope beam facilities (see, e.g., Refs. [12–19]) and, in parallel, the search for new production approaches is of great importance. Neutron-rich nuclides are produced by spallation, fission, and projectile fragmentation [20]. Spallation is an important mechanism to produce rare isotopes for isotope separator on-line (ISOL)-type techniques [21]. Projectile fission has proved to be a prolific production approach mainly in the region of light and heavy fission fragments (see, e.g., Ref. [22] for recent efforts on ^{238}U projectile fission). Finally, projectile fragmentation offers a very successful approach to produce a broad range of exotic nuclei at beam energies above 100 MeV/nucleon (see, e.g., Refs. [23,24] for recent work on projectile fragmentation). This approach is, nevertheless, based on the fact that optimum neutron excess in the fragments is achieved by stripping the maximum possible number of protons (and no neutrons, or a minimum possible number of neutrons).

To reach a very high neutron-excess in the products, apart from proton stripping, it may be necessary to capture neutrons from the target. Such a possibility is offered by reactions of nucleon exchange that prevail at beam energies from the Coulomb barrier [25,26] to the Fermi energy (20–40 MeV/nucleon) [27–30]. Detailed experimental data in this broad energy range are scarce at present, mostly due to the complex procedure of identification and separation [26,31,32] caused, primarily, by the wide charge state distribution of the reaction products. In multinucleon transfer and deep-inelastic reactions near the Coulomb barrier [26], the low velocities

of the fragments and the wide angular and ionic charge state distributions may limit the collection efficiency for the most neutron-rich products. The reactions in the Fermi energy regime [33] offer the opportunity to combine the advantages of both low-energy (i.e., near and above the Coulomb barrier) and high-energy (i.e., above 100 MeV/nucleon) reactions. At this energy, the synergy of both the projectile and the target enhances the N/Z of the fragments, while the fragment velocities are high enough to allow efficient in-flight collection and separation.

Our previous experimental studies of projectile fragments from the reactions of 25 MeV/nucleon ^{86}Kr on ^{64}Ni [29] and ^{124}Sn [30] indicated substantial production of neutron-rich fragments. The production mechanism was described by a deep-inelastic transfer model [34,35]. At this energy, neutron-rich fragments with up to four to five neutrons picked up from the target (along with the usual proton-removal fragments) were observed, demonstrating the important role of the target in the production mechanism.

After establishing that peripheral nucleon exchange can be adequately modeled via a deep-inelastic transfer approach [35], we proceeded to describe the literature data at low energies (near and above the Coulomb barrier) within the same deep-inelastic transfer framework [36]. We concluded that at these low energies, mainly due to longer interaction times, exchange of nucleons may take place in a very peripheral fashion, involving extended profiles of the reaction partners (forming a necklike structure during their interaction). This work also indicated the complete lack of production cross-section data at energies between the low-energy regime and the lower side of the Fermi energy range, i.e., near 25 MeV/nucleon.

To advance our understanding of the evolution of the reaction mechanisms and, furthermore, motivated by recent developments in several facilities that will offer either very intense primary beams [15,18,37] at this energy range or reaccelerated rare isotope beams [14,15,18,19], we undertook experimental studies at 15 MeV/nucleon and those studies are presented in this article. We believe that a clear understanding of the reaction mechanisms at this energy range and a reliable model framework for the production cross sections will allow us to select the proper separator configuration (see, e.g., Refs. [38–40]) and the optimum projectile/target combinations (as well as the appropriate target thickness) for efficient production and collection of very neutron-rich exotic nuclei.

This article presents mass spectrometric measurements of production cross sections of neutron-rich projectile fragments from the reactions of a 15 MeV/nucleon ^{86}Kr beam with ^{64,58}Ni and ^{124,112}Sn targets and comparisons with our earlier data at 25 MeV/nucleon. The article is organized as follows: In Sec. II a detailed description of the experimental setup, the measurements, and the data analysis are given. In Sec. III, the procedure to obtain total production cross sections from the measured data is presented. In Sec. IV, the results on isotope distributions with emphasis on the neutron-rich nuclides are discussed. Finally, in Sec. V, a summary and conclusions are given.

II. EXPERIMENTAL METHOD AND DATA ANALYSIS

The present study was performed at the Cyclotron Institute of Texas A&M University following the experimental scheme of our previous work [29–31]. A 15 MeV/nucleon ^{86}Kr beam from the K500 superconducting cyclotron, with a typical current of 5 pnA (3.1×10^{10} particles/s), interacted with isotopically enriched targets of ^{64}Ni and ^{58}Ni (with thickness 4 mg/cm^2) and ^{124}Sn and ^{112}Sn (with thickness 2 mg/cm^2).

The reaction products were analyzed with the momentum achromat recoil separator (MARS) [41]. The experimental setup is schematically shown in Fig. 1. The MARS optics provides one intermediate dispersive image and a final achromatic image. The maximum angular acceptance is 9 msr and the momentum acceptance is 4%. In the present measurements, as in our previous work at 25 MeV/nucleon, the Wien filter of the MARS was not used and the last section of the device (after the dipole D3) was set at 0°. The primary beam hit the target at an angle with respect to the optical axis of the MARS (see below). The unreacted beam was collected on a Faraday cup inside the target chamber. An Al foil (1 mg/cm^2) was positioned at the entrance of the spectrometer to reset to equilibrium the ionic charge states of the reaction products.

To ensure uniform transmission of the fragments through the MARS, the horizontal and vertical slits at the entrance of the first quadrupole (Q1) were restricted to a 2×2 cm window (at a distance of 31.5 cm from the target). This window defined a horizontal angular acceptance of $\Delta\theta = 3.6°$ ($\pm 1.8°$) and similarly a vertical angular acceptance of $\Delta\phi = 3.6°$, thus allowing a solid angle of $\Delta\Omega = 4.0$ msr. To cover a wide angular range for the reactions studied, the experiment was divided in two parts. In the first part, the primary beam struck the target at an angle of 4.0° relative to the optical axis of the spectrometer and, thus, fragments were accepted in the angular range of 2.2°–5.8°. In the second part, the beam hit the target at an angle of 7.4° and the fragments were collected in the angular range of 5.6°–9.2°. In the following, we refer to the data taken at these two experimental parts as the "4° data" and the "7° data," respectively. We consider the two horizontal angular ranges as adjacent, ignoring the small overlap between them
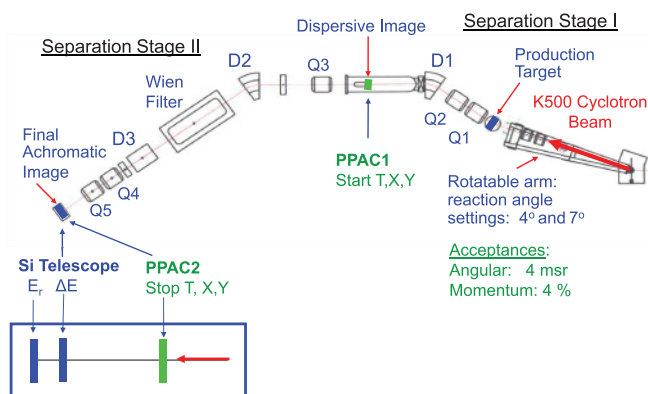

FIG. 1. (Color online) Schematic diagram of the MARS experimental setup for rare isotope production. The main elements of the MARS ("Q" for quadrupoles, "D" for dipoles) and the location of the detectors are indicated (see text).

(that is comparable to the accuracy of determination of the geometrical parameters of the experimental setup). We verified that full transmission of the ions through the spectrometer was achieved using a Rutherford scattered beam of ^{86}Kr on a ^{197}Au target at both angular settings of the spectrometer (4° and 7° settings).

The full angular range of 2.2°–9.2° corresponding to the combined 4° and 7° data covers most of the angular distribution of projectile fragments from the reactions with the Ni targets, ^{86}Kr + ^{64,58}Ni, which have a grazing angle of 6.0° [42]. The reactions with the Sn targets, ^{86}Kr + ^{124,112}Sn, have a grazing angle of 9.0° [42].

Thus, the angular range in which the data were obtained lies inside the grazing angle of this system (where the yield of near-projectile fragments is expected to be maximum).

Time of flight of the fragments was measured between two PPACs (parallel plate avalanche counters) [43] positioned at the dispersive image (PPAC1) and at the final image (PPAC2), respectively, and separated by a distance of 13.2 m. Both PPACs were also X-Y position sensitive and this information was used to monitor the focusing and collection of the fragments at the various magnetic rigidity settings of the separator. In particular, the horizontal position of PPAC1 (at the dispersive image), along with NMR measurements of the field of the MARS's first dipole, was used to determine the magnetic rigidity $B\rho$ of the particles. At the final achromatic image, projectile fragments were collected in a large area (5 × 5 cm) two-element (ΔE, E) Si detector telescope. The thicknesses of the detectors were 70 and 1000 μm, respectively.

Thus, projectile fragments were characterized by event-by-event measurements of energy loss ΔE (in the first Si detector), residual energy E_r (in the second Si detector), time of flight, and magnetic rigidity. The response of the spectrometer/detector system to ions of known atomic number Z, mass number A, ionic charge q, and velocity was calibrated using low-intensity primary beams of ^{40}Ar and ^{86}Kr at 15 MeV/nucleon (and lower energies achieved with Al targets of several thicknesses). These calibration beams were sent at an angle of 0° with respect to the optical axis of the MARS.

To cover the N/Z and velocity range of the fragments, at each part of the experiment, a series of measurements was performed at overlapping magnetic rigidity settings in the range 1.1–2.0 Tm. This magnetic rigidity range was adequate to fully cover the velocity and ionic charge distributions of fragments near the projectile.

The determination of the atomic number Z [44] was based on the energy loss ΔE of the particles in the first Si detector [45,46] and their velocity, with a resulting resolution (FWHM) of 0.5 Z units for near-projectile fragments. The ionic charge q of the particles after the Al stripper was obtained from the total energy $E_{tot} = \Delta E + E_r$, the velocity v, and the magnetic rigidity $B\rho$ according to the expression

$$q = \frac{3.107}{931.5} \frac{E_{tot}}{B\rho(\gamma - 1)} \beta\gamma, \tag{1}$$

where E_{tot} is in MeV, $B\rho$ in Tm, $\beta = v/c$, and $\gamma = 1/(1 - \beta^2)^{\frac{1}{2}}$. The resulting ionic charge q had a resolution of 0.4 units (FWHM). Since the ionic charge must be an integer, we assigned integer values of q for each event by setting windows

($\Delta q = 0.4$) on each peak of the q spectrum at each magnetic rigidity setting of the spectrometer. Using the magnetic rigidity and velocity measurements, the mass-to-charge A/q ratio of each ion was calculated from the expression

$$A/q = \frac{B\rho}{3.107\beta\gamma} \tag{2}$$

Combining the ionic charge q determination with the A/q measurement, the mass number A was obtained as

$$A = q_{int} \times A/q \tag{3}$$

(q_{int} is the integer ionic charge determined as described above) with an overall resolution (FWHM) of about 0.6 A units. The reconstruction of the Z, q, and A and the gating procedure (windows of 0.5 and 0.4 units in the Z and q peaks, respectively) were applied to the calibration beam data to ensure the reproduction of the expected Z, q, and A values and the elimination of spurious yield contributions from neighboring Z and q values.

Combination and appropriate normalization of the data (with the aid of the measured beam current) at the various magnetic rigidity settings of the spectrometer provided fragment distributions with respect to Z, A, q, and velocity. Correction of missing yields caused by resetting to equilibrium (and, thus, changing) each charge state passing through PPAC1 (at the dispersive image) was performed based on the equilibrium charge state parametrizations of Leon *et al.* [47]. The isotope distributions were subsequently summed over all values of q and scaled with respect to beam current, target thickness, and solid angle ($\Delta\Omega = 4.0$ msr) for each of the two angle settings of the spectrometer. Thus, the resulting fragment distributions in Z, A, and velocity represent the differential cross sections measured at the two angle intervals (2.2°–5.8° for the 4° data and 5.6°–9.2° for the 7° data) in the magnetic rigidity range $B\rho = 1.1$–2.0 Tm.

Summing over velocity provided distributions with respect to Z and A. Furthermore, for each fragment, the two differential cross sections were scaled by the corresponding azimuthal factors (a factor of 7 for the 4° data and a factor of 13 for the 7° data) and summed to provide the intergrated cross section at the full angular range (2.2°–9.2°) covered in the measurements.

III. FRAGMENT MASS DISTRIBUTIONS AND TOTAL PRODUCTION CROSS SECTIONS

In Figs. 2 and 3, the fragment differential cross sections as a function of mass at 4° and 7° are shown by the diamond and triangle points, respectively.

For the ^{86}Kr + ^{64}Ni reaction having a grazing angle of $\theta_{gr} = 6.0°$, the differential cross sections at the 4° setting are larger than those at the 7° setting. This is to be expected, since the peak of the production cross section lies in the angle interval just inside the grazing angle [33]. For the ^{86}Kr + ^{124}Sn reaction ($\theta_{gr} = 9.0°$), the differential cross sections for near-projectile fragments obtained at the 7° setting are larger than those at the 4° setting, since now the 7° angle interval lies just inside the grazing angle of this system. The integrated cross sections in the full angle interval 2.2°–9.2° (obtained from the measured
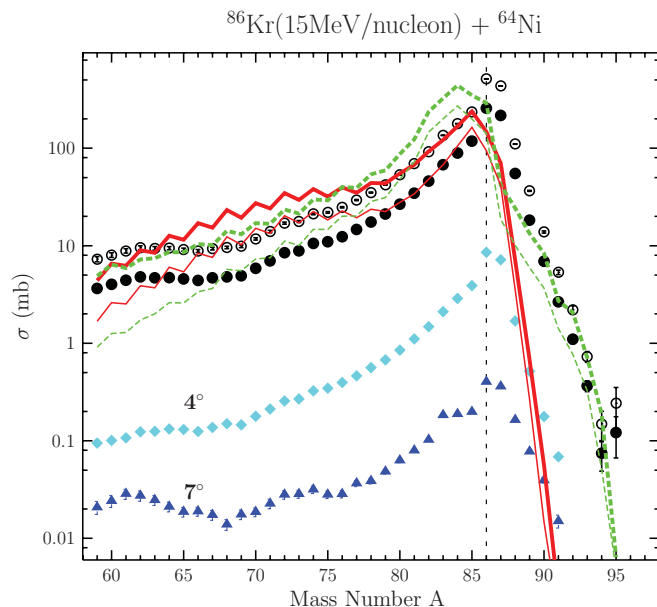
^{86}Kr(15MeV/nucleon) + ^{64}Ni

^{86}Kr(15MeV/nucleon) + ^{124}Sn

FIG. 2. (Color online) Mass distributions of projectilelike fragments from the reaction of ^{86}Kr (15 MeV/nucleon) with ^{64}Ni. The vertical dashed line indicates the mass of the projectile. Diamonds: Measured differential cross sections (mb/msr) at 4°. Triangles: Measured differential cross sections at 7°. Solid circles: Cross sections (mb) from the combined data at 4° and 7°. Open circles: Total cross sections (mb), (i.e., measured cross sections corrected for the acceptance of the measurements with the MARS). Solid lines: DIT/GEMINI calculations. Dashed lines: CoMD/GEMINI calculations. For each model calculation, thick lines represent total cross sections and thin lines are cross sections filtered by the acceptance of the experimental setup (see text).

FIG. 3. (Color online) Mass distributions of projectilelike fragments from the reaction of ^{86}Kr (15 MeV/nucleon) with ^{124}Sn. The meanings of the points and lines are as in Fig. 2.

differential cross sections as explained above) are shown by the solid circles in Figs. 2 and 3.

While a broad part of the angular distributions of near-projectile fragments is covered in the present measurements, the integrated cross sections shown in Figs. 2 and 3 are, of course, not total production cross sections. To establish what fraction of the distributions was covered in the measurements (and use this information to obtain total production cross sections), we had to resort to reaction simulations employing appropriate models.

The calculations performed in this work are based on a two-stage Monte Carlo approach. The dynamical stage of the collisions was described by two different models: First, we used the phenomenological deep-inelastic transfer (DIT) model [34] simulating stochastic nucleon exchange in peripheral and semiperipheral collisions. This model has been successful in describing the N/Z, excitation energy, and kinematic properties of excited quasiprojectiles in a number of recent studies [27–30,35,36]. We also employed the microscopic constrained molecular dynamics (CoMD) model [48,49] successfully used in studies from low energies to the Fermi energy regime [48,50,51]. This code, following the general approach of the quantum molecular dynamics (QMD) models [52], implements an effective nucleon-nucleon interaction with a nuclear-matter compressibility of $K = 200$
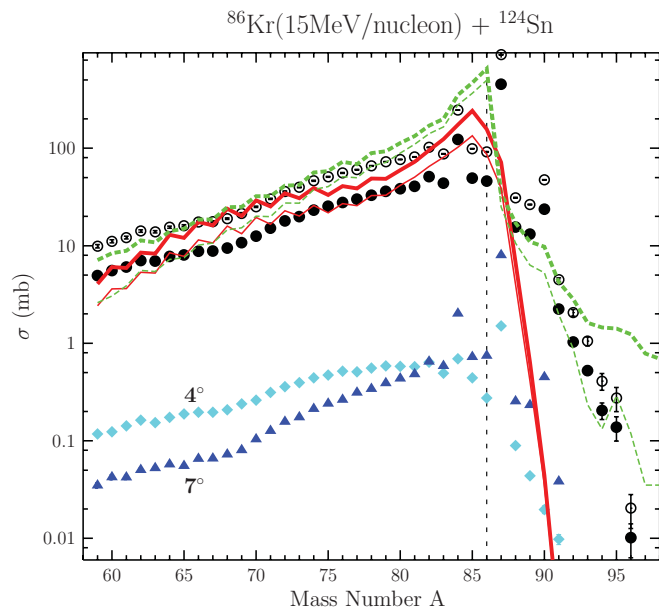
(soft EOS) and several forms of the density dependence of the nucleon-nucleon symmetry potential. Moreover, it imposes a phase space constraint to restore the Pauli principle during the collision. Our recent studies at 25 MeV/nucleon [50] are consistent with a rather stiff density dependence of the symmetry energy (more precisely, a symmetry potential proportional to density), in good agreement with other studies [51]. In the present CoMD calculations, the dynamical evolution of the system was stopped at $t = 300$ fm/c. After the dynamical stage as simulated by DIT or CoMD, the deexcitation stage of the reaction was described by the statistical code GEMINI [53,54]. This deexcitation code employs Monte Carlo techniques and the Hauser-Feshbach formalism to calculate the probabilities for fragment emission with $Z \leqslant 2$. Heavier fragment emission probabilities are calculated via a transition state formalism.

We wish to point out that our recent work employing the codes DIT/GEMINI and CoMD/GEMINI [50] provided a rather reasonable description of the production cross sections and velocity distributions of near-projectile residues at 25 MeV/nucleon. We thus applied these model frameworks with some confidence in the present reactions at 15 MeV/nucleon. In Figs. 2 and 3, the total production cross sections as a function of mass, as predicted by DIT/GEMINI, are given by the thick solid lines for the ^{86}Kr + ^{64}Ni and ^{86}Kr + ^{124}Sn reactions, respectively. Similarly, the CoMD/GEMINI results are shown by thick dashed lines. Subsequently, both calculations were filtered for the angular acceptance $\Delta\theta = 2.2°–9.2°$ and magnetic rigidity $B\rho = 1.1–2.0$ Tm covered by the experiment and the results are given by the thin full line for the DIT/GEMINI calculation and the thin dashed line for the CoMD/GEMINI calculation. We observe that for fragments very close to the projectile, the filtered DIT/GEMINI calculation seems to describe the data better than the CoMD/GEMINI

calculation. Nonetheless, the CoMD/GEMINI simulation (thin dashed lines) appears to better describe the "transprojectile" residues (with $A > 86$, resulting from picking up of protons and neutrons from the target).

We used the ratio of the filtered to the unfiltered yields to obtain an estimate of the fraction of the total cross section for each fragment that was covered in our measurements. We point out that this ratio depends on both the A and the Z of the fragments. We can easily estimate this ratio for each mass from the displacement of the thick lines relative to the thin lines in Figs. 2 and 3. For the subsequent discussion, and to avoid dependence on the details of the models used in our simulations, we considered this ratio to be 0.5 for the fragments of interest from both reactions. Thus the measured integrated cross sections were further multiplied by a factor of 2.0 to provide the total production cross sections for each fragment. We estimate that the uncertainty in the total production cross sections obtained with the above procedure is approximately a factor of 2. We also note that the error bars presented in the following results are only statistical.

IV. RESULTS ON NEUTRON-RICH RARE ISOTOPE PRODUCTION

In Figs. 4 and 5, we present the extracted production cross sections for each isotope of the elements $Z = 35$–30 from the reactions of ^{86}Kr (15 MeV/nucleon) with ^{64}Ni and ^{58}Ni, and also for the reactions of ^{86}Kr (15 MeV/nucleon) with ^{124}Sn and ^{112}Sn, respectively. Solid circles correspond to the reactions with the neutron-rich targets and open circles to those of the neutron-deficient targets. We wish to point out that the cross sections presented in this section result from the combination of the 4° data and the 7° data (as mentioned in the previous section) multiplied furthermore by the overall factor of 2 to correct for the limited angular range of the experimental measurement. We observe that for fragments close to the projectile (e.g., $Z = 35$ and 34) neutron pickup products are present with up to six neutrons picked up from the target. As expected, the yields of fragments from the reactions with the neutron-rich targets are, in general, larger relative to those from the reactions with the neutron-poor targets [30].
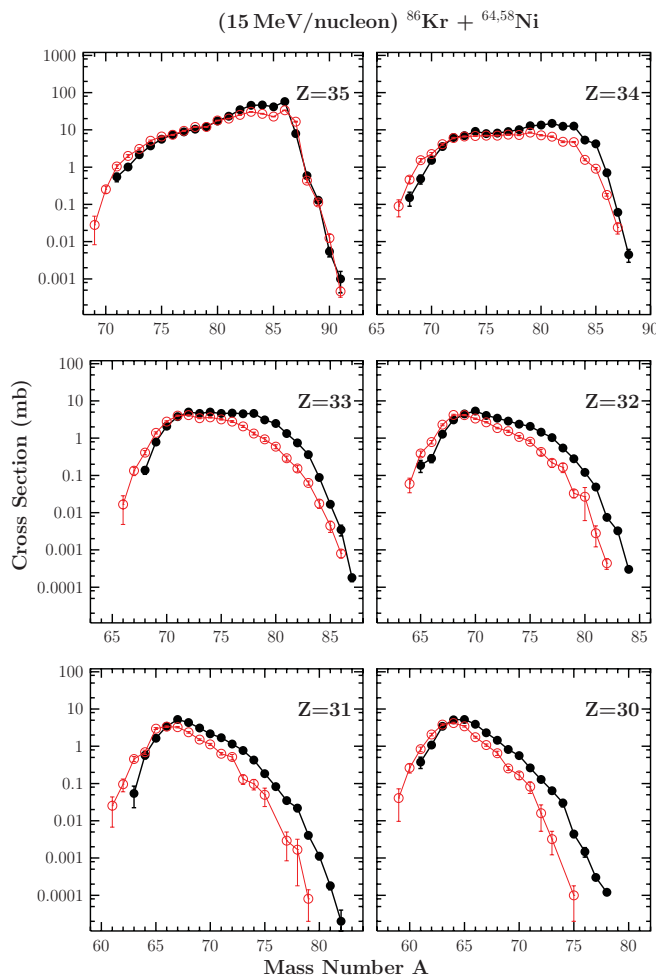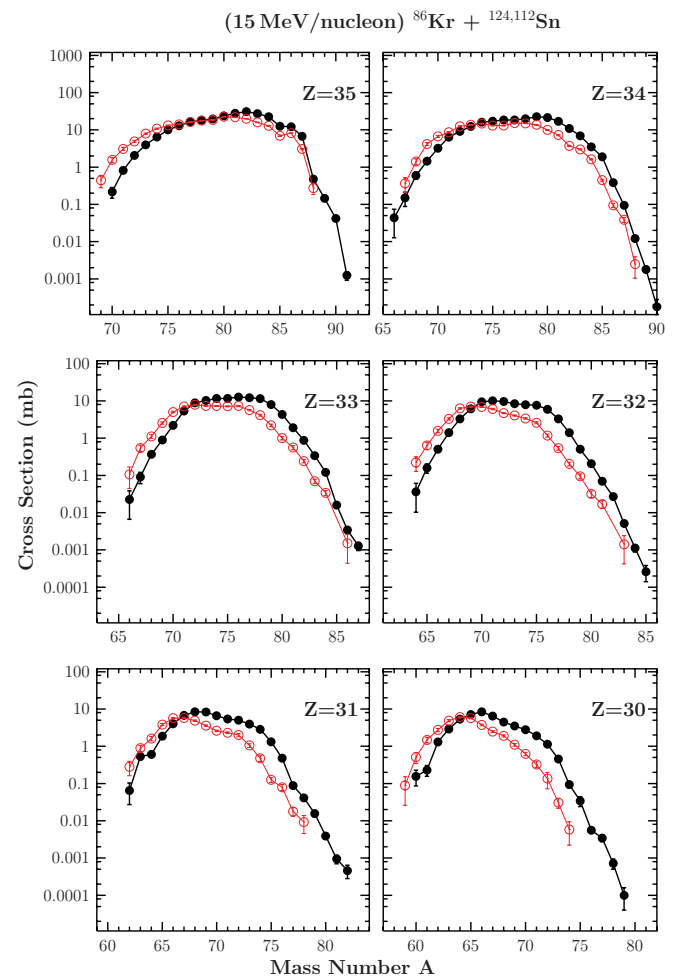

FIG. 4. (Color online) Mass distributions of elements $Z = 35$–30 from the reactions of ^{86}Kr (15 MeV/nucleon) with ^{64}Ni and ^{58}Ni. The data are shown by solid circles for ^{86}Kr + ^{64}Ni and open circles for ^{86}Kr + ^{58}Ni.

FIG. 5. (Color online) Mass distributions of elements $Z = 35$–30 from the reactions of ^{86}Kr (15 MeV/nucleon) with ^{124}Sn and ^{112}Sn. The data are shown by solid circles for ^{86}Kr + ^{124}Sn and open circles for ^{86}Kr + ^{112}Sn.
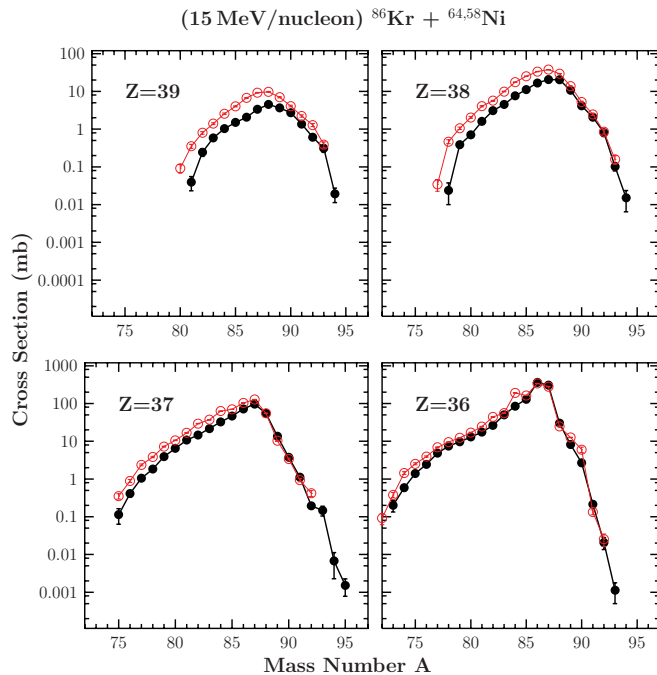
FIG. 6. (Color online) Mass distributions of elements $Z = 36\text{--}39$ from the reactions of ^{86}Kr (15 MeV/nucleon) with ^{64}Ni and ^{58}Ni. The data are shown by solid circles for ^{86}Kr $+$ ^{64}Ni and open circles for ^{86}Kr $+$ ^{58}Ni.

In Fig. 6, the production cross sections of the isotopes with $Z = 36\text{--}39$ from the reaction of ^{86}Kr (15 MeV/nucleon) with ^{64,58}Ni are presented. We note that the Kr isotopes ($Z = 36$) include products with up to seven neutrons picked up from the target. It is interesting to observe the production of multinucleon transfer products with several protons and neutrons picked up from the target at this energy. Similar behavior has been observed for the transprojectile residues from the reaction of ^{86}Kr (15 MeV/nucleon) with ^{124,112}Sn. As hinted by Figs. 2 and 3, the CoMD/GEMINI simulation appears to describe to some extent the isobaric yield distributions of these products, whereas the DIT/GEMINI simulation is not able to do so. Understanding the details of the production mechanism of these transprojectile isotopes is important for the application of such reactions in the production of very neutron-rich isotopes of heavy elements [39,40] and will be the subject of future experimental and theoretical work. Moreover, efforts on the systematic investigation of the production, especially of the neutron-rich products employing the model frameworks mentioned above, are currently ongoing.

In Fig. 7, we present a comparison of the present data (solid circles) of ^{86}Kr (15 MeV/nucleon) $+$ ^{64}Ni with our previous work [29] on the same reaction at 25 MeV/nucleon (solid diamonds). In this figure we also show the cross sections that correspond to high-energy projectile fragmentation of ^{86}Kr on ^{64}Ni as predicted by the empirical parametrization EPAX [55]. We remind the reader that, in high-energy fragmentation, nucleon-pickup products are not produced or, at best, are highly suppressed compared to lower energy peripheral collisions. Interestingly, we observe that the reaction at 15 MeV/nucleon results in much larger cross sections for
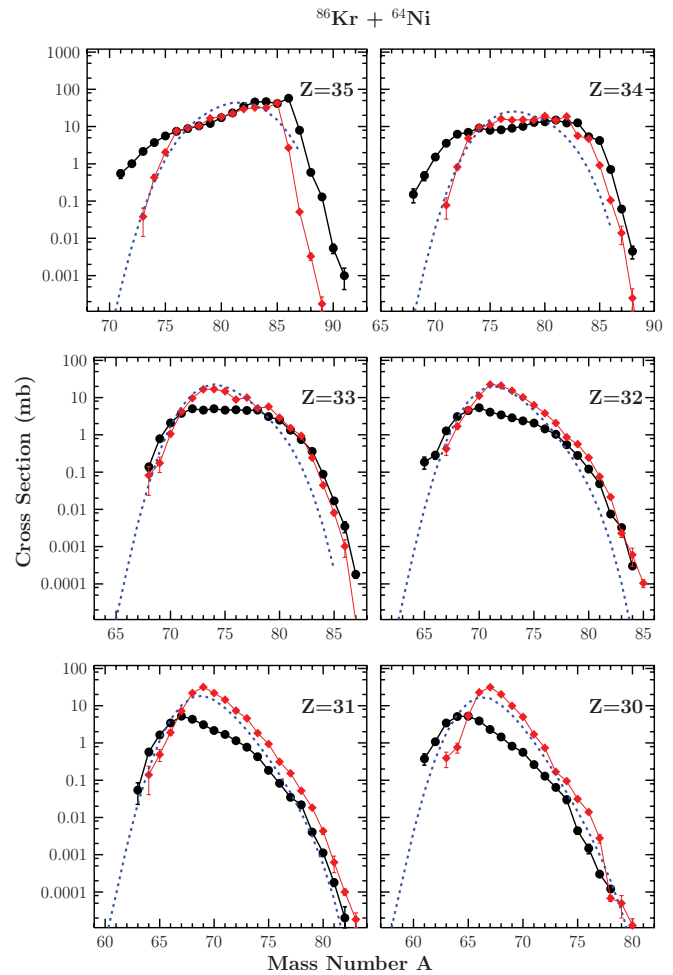

FIG. 7. (Color online) Comparisons of mass distributions of elements $Z = 35\text{--}30$ from the reaction of ^{86}Kr with ^{64}Ni at 15 MeV/nucleon of this work (circles) with those of our previous work [29] at 25 MeV/nucleon (diamonds). The dotted lines are the EPAX expectations [55].

products very close to the projectile. As we see, for example, for Br ($Z = 35$), the most neutron-rich neutron-pickup isotopes are by a factor of 10 (or larger) more abundantly produced at 15 MeV/nucleon than at 25 MeV/nucleon. As we move further from the projectile (to lower Z elements), the cross sections of the most neutron-rich products appear to be nearly similar between the two energies. Even if a quantitative interpretation effort is the subject of upcoming work, qualitatively we can say that for the reactions at 15 MeV/nucleon, lower excitation energies of the primary fragments and larger interaction times for the most peripheral collisions may be responsible for the production and survival of residues with a large number of neutrons picked up from the target. For elements further from the projectile, the production of neutron-rich species may require a larger number of nucleons exchanged between the projectile and the target and, thus, these products possibly result from quasiprojectiles at nearly similar excitation energies, ending up with comparable cross sections at the two energies.
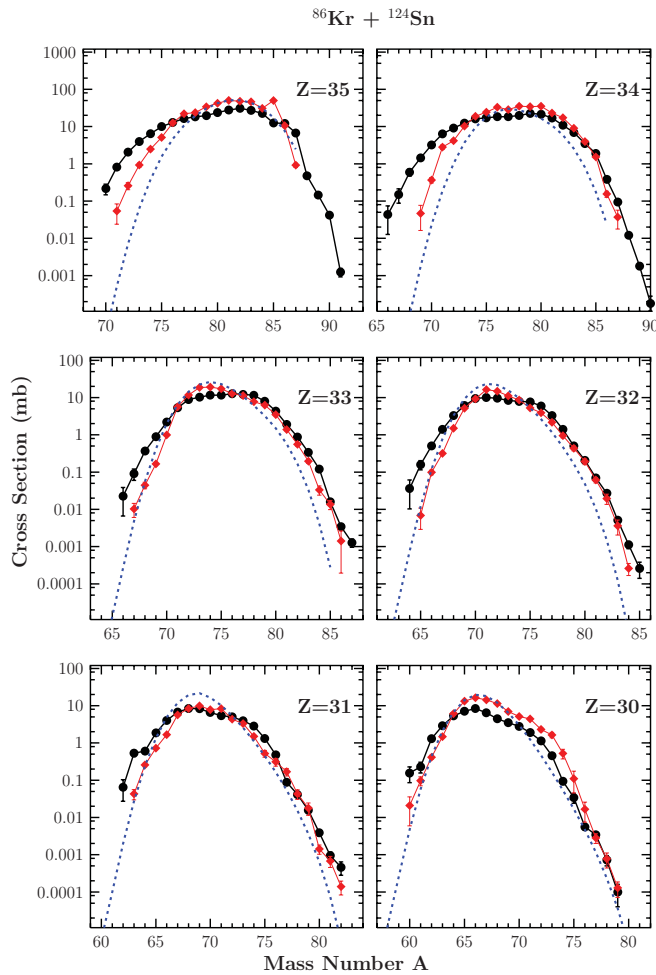
^{86}Kr + ^{124}Sn

FIG. 8. (Color online) Comparisons of mass distributions of elements $Z = 35$–30 from the reaction of ^{86}Kr with ^{124}Sn at 15 MeV/nucleon of this work (circles) with those of our previous work [29] at 25 MeV/nucleon (diamonds). The dotted lines are the EPAX expectations [55].

We also observe (Fig. 7) that for fragments further from the projectile, for example, As ($Z = 33$) and below, the production cross sections at the peaks of the distributions are lower at 15 MeV/nucleon as compared to those at 25 MeV/nucleon. We may qualitatively interpret this observation as an effect of the overall lower excitation energies of the quasiprojectiles obtained at 15 MeV/nucleon relative to those at 25 MeV/nucleon. The result is preferential neutron evaporation at the former energy (notice also the larger neutron-deficient tails for $Z = 35$ and $Z = 34$), as compared to the more extended proton and light-charged-particle evaporation (as well as sequential binary decay) leading to products at lower Z and closer to the line of β stability at the latter energy.

Similar observations pertain to the comparison of the 15 MeV/nucleon ^{86}Kr + ^{124}Sn data to our earlier work on the same reaction at 25 MeV/nucleon [30], as presented in Fig. 8 (circles and diamonds, respectively). However, we note that the 25 MeV/nucleon data [30] do not contain the most neutron-rich products close to the projectile. Also, for fragments further from the projectile (e.g., $Z = 33$ and 32)
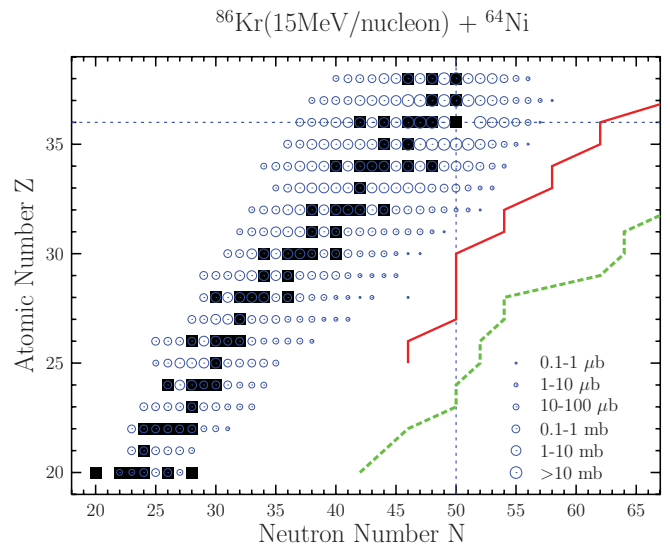
^{86}Kr(15MeV/nucleon) + ^{64}Ni

FIG. 9. (Color online) Representation of the production cross sections of projectile fragments from the reaction ^{86}Kr (15 MeV/nucleon) + ^{64}Ni on the Z-N plane. The cross-section ranges are shown by open circles according to the key. The solid squares show the stable isotopes. The solid line shows the astrophysical r-process path and the dashed line shows the location of the neutron drip-line [56]. The horizontal and vertical dashed lines indicate, respectively, the proton and neutron number of the ^{86}Kr projectile.

the distributions are similar at their central and neutron-rich parts. For this system involving a heavier target, the excitation energy distributions of the primary quasiprojectiles that lead to the observed projectilelike fragments may be similar at the two energies.

A comprehensive presentation of the production cross sections of the projectilelike fragments from the 15 MeV/nucleon reactions ^{86}Kr + ^{64}Ni and ^{86}Kr + ^{124}Sn on the Z vs N plane is given in Figs. 9 and 10. In these figures, stable isotopes are represented by solid squares, whereas fragments obtained in this work are given by the open circles (with sizes corresponding to cross-section ranges according to the figure key). The dashed line gives the location of the neutron drip-line and the solid line indicates the expected path of the astrophysical rapid neutron-capture process (r-process), as calculated in Ref. [56]. In these figures we observe that the neutron pickup products from the ^{86}Kr projectile approach the path of the r-process near $Z = 32$–34. We can expect that an increase of the production rates by about 10^3 (by a factor of 100–200 in beam intensity and 5–10 in target thickness) may allow accessing the r-process path nuclei in the region $Z = 30$–36.

Thus, from a practical standpoint, we may conclude that the large production cross section of neutron-rich nuclides and, especially, the multineutron pickup possibility can render these reactions a promising route to produce extremely neutron-rich nuclides near and potentially beyond the r-process path. We remind that neutron pickup cross sections are also large in the case of multinucleon transfer reactions close to the Coulomb barrier [26]. However, these reactions have very wide angular, velocity, and ionic charge distributions, in addition
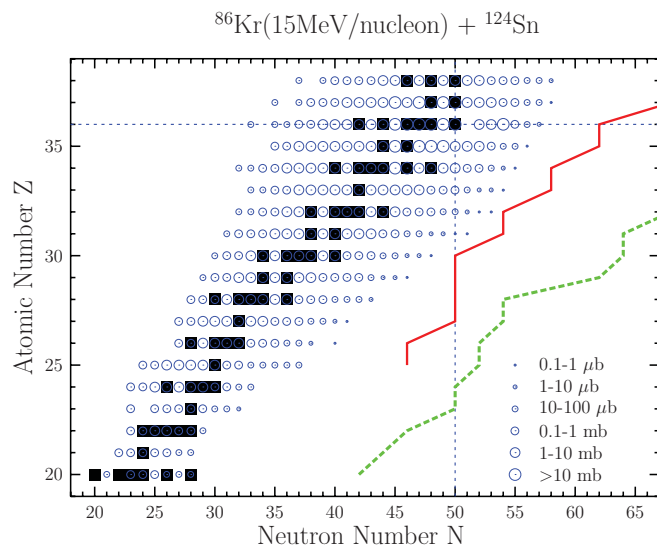
^{86}Kr(15MeV/nucleon) + ^{124}Sn

FIG. 10. (Color online) Representation of the production cross sections of projectile fragments from the reaction ^{86}Kr (15 MeV/nucleon) + ^{124}Sn on the Z-N plane. The cross-section ranges are shown by open circles according to the key. The solid squares show the stable isotopes. The solid line shows the astrophysical r-process path and the dashed line shows the location of the neutron drip-line [56]. The horizontal and vertical dashed lines indicate, respectively, the proton and neutron number of the ^{86}Kr projectile.

TABLE I. Cross sections and rate estimates (last column) of very neutron-rich isotopes from the reaction ^{86}Kr (15 MeV/nucleon) + ^{64}Ni. For the rates, the cross-section data of this work are used, and a primary beam of ^{86}Kr with intensity 500 pnA (3.1×10^{12} particles/s) is assumed to interact with a ^{64}Ni target of 20 mg/cm^2 thickness (see text).

Rare isotope	Reaction channel	Cross section	Rate (s^{-1})
^{90}Kr	$-0p + 4n$	2.7 mb	1.6×10^6
^{91}Kr	$-0p + 5n$	0.21 mb	1.3×10^5
^{92}Kr	$-0p + 6n$	20 μb	1.2×10^4
^{93}Kr	$-0p + 7n$	1.1 μb	7×10^2
^{87}Br	$-1p + 2n$	8.0 mb	4.8×10^6
^{88}Br	$-1p + 3n$	0.59 mb	3.5×10^5
^{89}Br	$-1p + 4n$	0.13 mb	7.8×10^4
^{90}Br	$-1p + 5n$	5.4 μb	3.2×10^3
^{91}Br	$-1p + 6n$	1.0 μb	6×10^2
^{84}Se	$-2p + 0n$	5.3 mb	3.2×10^6
^{85}Se	$-2p + 1n$	4.2 mb	2.5×10^6
^{86}Se	$-2p + 2n$	0.71 mb	4.2×10^5
^{87}Se	$-2p + 3n$	60 μb	3.6×10^4
^{88}Se	$-2p + 4n$	4.4 μb	2.6×10^3
^{83}As	$-3p + 0n$	0.36 mb	2.2×10^5
^{84}As	$-3p + 1n$	88 μb	5.3×10^4
^{85}As	$-3p + 2n$	17 μb	1.0×10^4
^{86}As	$-3p + 3n$	3.4 μb	2.0×10^3
^{87}As	$-3p + 4n$	0.2 μb	1.2×10^2
^{82}Ge	$-4p + 0n$	7.4 μb	4.4×10^3
^{83}Ge	$-4p + 1n$	3.2 μb	1.9×10^3
^{84}Ge	$-4p + 2n$	0.3 μb	1.8×10^2

to the necessity of rather thin targets (around 1 mg/cm^2). At this higher energy, however, inverse kinematic reactions have angular and ionic charge state distributions that can be efficiently collected using a large acceptance spectrometer [38,39]. Also the energy is high enough to allow thicker targets (10–20 mg/cm^2). Using the present cross sections, we can make estimates of rare isotope production rates from intense beams at this energy that will become available at several facilities (e.g., Refs. [15,18]). As examples, we present in Table I the cross sections and production rates for the most neutron-rich nuclides from Kr ($Z = 36$) to Ge ($Z = 32$). The cross sections of this work are given in the third column. The last column of the table gives the expected rates calculated using the present cross sections and assuming a beam of 500 pnA ^{86}Kr at 15 MeV/nucleon striking a 20 mg/cm^2 ^{64}Ni target. Such yields of very neutron-rich isotopes will enable a variety of nuclear structure and nuclear reaction studies at this energy.

Finally, another promising possibility is the use of such reactions as a second stage in two-stage rare isotope production schemes. For example, a beam of ^{92}Kr from an ISOL facility can be accelerated at 15 MeV/nucleon and subsequently strike a ^{64}Ni target to produce very neutron-rich nuclides that may be separated and studied in flight. To estimate the rates of such reaction products, the cross sections of this work may be used as a rough approximation. However, a quantitative prediction will be possible after obtaining an adequate theoretical description of these peripheral collisions between neutron-rich nuclei at this energy, which is one of the goals of upcoming work.

V. SUMMARY AND CONCLUSIONS

In summary, the present work described the mass spectrometric measurements of the production cross sections of projectilelike fragments from the reactions of 15 MeV/nucleon ^{86}Kr with ^{64,58}Ni and ^{124,112}Sn. The measurements were performed in a wide angular range near the grazing angle of the systems. Special emphasis was given to the neutron-rich isotopes. Along with the usual proton-removal products, neutron pickup isotopes (with up to six or seven neutrons picked up from the target) were observed with large cross sections. Calculations involving the DIT model as well as the microscopic CoMD model for the primary interaction stage combined with the deexcitation code GEMINI were employed to describe the isobaric distributions of the fragments. The present experimental results were also compared to our previous data of the same reactions at 25 MeV/nucleon [29,30]. The data at 15 MeV/nucleon show enhanced production of neutron-rich isotopes very close to the projectile, relative to the corresponding data at 25 MeV/nucleon. This enhancement in the cross sections may be associated with very peripheral collisions and long interaction times of the neutron-rich ^{86}Kr projectile with the neutron-rich targets. Such reactions well above the Coulomb barrier, but below the Fermi energy, involving peripheral nucleon exchange, offer a new approach to access extremely neutron-rich rare isotopes toward the r-process path and, potentially, the neutron drip-line.

[1] J. Äystö, W. Nazarewicz, M. Pfützner, and C. Signorini (Editors), in *Proceedings of the Fifth International Conference on Exotic Nuclei and Atomic Masses (ENAM'08), Ryn, Poland, September 7–13 2008)* [Eur. Phys. J. A, **42** (2009)].

[2] C. Sneden and J. J. Cowan, Science **299**, 70 (2003).

[3] K. Langanke and M. Wiescher, Rep. Prog. Phys. **64**, 1657 (2001).

[4] H.-T. Janka, K. Langanke, A. Marek, G. Martínez-Pinedo, and B. Müller, Phys. Rep. **442**, 38 (2007).

[5] P. Danielewicz, R. Lacey, and W. G. Lynch, Science **298**, 1592 (2002).

[6] B.-A. Li, L. W. Chen, and C. M. Ko, Phys. Rep. **464**, 113 (2008).

[7] D. V. Shetty, S. J. Yennello, and G. A. Souliotis, Phys. Rev. C **76**, 024606 (2007).

[8] V. Baran *et al.*, Phys. Rep. **410**, 335 (2005).

[9] A. R. Raduta and F. Gulminelli, Phys. Rev. C **82**, 065801 (2010).

[10] C. J. Pethick and D. G. Ravenhall, Annu. Rev. Nucl. Part. Sci. **45**, 429 (1995).

[11] J. M. Lattimer and M. Prakash, Phys. Rep. **442**, 109 (2007).

[12] *Scientific Opportunities with a Rare-Isotope Facility in the United States* (National Academies Press, Washington, DC, 2007).

[13] D. F. Geesaman, C. K. Gelbke, R. V. F. Janssens, and B. M. Sherrill, Annu. Rev. Nucl. Part. Sci. **56**, 53 (2006).

[14] FRIB main page [www.frib.msu.edu].

[15] GANIL main page [www.ganil.fr].

[16] GSI main page [www.gsi.de].

[17] RIBF main page [www.rarf.riken.go.jp/Eng/facilities/RIBF.html].

[18] ATLAS main page [www.phy.anl.gov/atlas/facility/index.html].

[19] EURISOL main page [www.eurisol.org].

[20] H. Geissel and G. Munzenberg, Annu. Rev. Nucl. Part. Sci. **45**, 163 (1995).

[21] A. Kelić, M. V. Ricciardi, and K. H. Schmidt, Bulgarian Nuclear Society Transactions **13**, 98 (2009).

[22] H. Alvarez-Pol *et al.*, Phys. Rev. C **82**, 041602 (2010).

[23] O. B. Tarasov *et al.*, Phys. Rev. C **80**, 034609 (2009).

[24] S. Lukyanov *et al.*, Phys. Rev. C **80**, 014609 (2009).

[25] V. V. Volkov, Phys. Rep. **44**, 93 (1978).

[26] L. Corradi, G. Pollarolo, and S. Szilner, J. Phys. G **36**, 113101 (2009).

[27] M. Veselsky *et al.*, Phys. Rev. C **62**, 064613 (2000).

[28] M. Veselsky *et al.*, Nucl. Phys. A **705**, 193 (2002).

[29] G. A. Souliotis *et al.*, Phys. Lett. B **543**, 163 (2002).

[30] G. A. Souliotis *et al.*, Phys. Rev. Lett. **91**, 022701 (2003).

[31] G. A. Souliotis *et al.*, Nucl. Instrum. Methods Phys. Res., Sect. B **204**, 166 (2003).

[32] G. A. Souliotis *et al.*, Nucl. Instrum. Methods Phys. Res., Sect. B **266**, 4692 (2008).

[33] H. Fuchs and K. Möhring, Rep. Prog. Phys. **57**, 231 (1994).

[34] L. Tassan-Got and C. Stefan, Nucl. Phys. A **524**, 121 (1991).

[35] M. Veselsky and G. A. Souliotis, Nucl. Phys. A **765**, 252 (2006).

[36] M. Veselsky and G. A. Souliotis, Nucl. Phys. A **872**, 1 (2011).

[37] Texas A&M Cyclotron Institute main page [cyclotron.tamu.edu].

[38] G. A. Souliotis *et al.*, Nucl. Instrum. Methods Phys. Res., Sect. B **266**, 4213 (2008).

[39] A. Druart *et al.*, Nucl. Instrum. Methods Phys. Res., Sect. B **266**, 4162 (2008).

[40] J. Dvorak *et al.*, Nucl. Instrum. Methods Phys. Res., Sect. A (2011).

[41] R. E. Tribble, R. H. Burch, and C. A. Gagliardi, Nucl. Instrum. Methods A **285**, 441 (1989).

[42] W. W. Wilcke *et al.*, At. Data Nucl. Data Tables **25**, 389 (1980).

[43] D. Swan, J. Yurkon, and D. J. Morrissey, Nucl. Instrum. Methods A **348**, 314 (1994).

[44] G. A. Souliotis, K. Hanold, W. Loveland, I. Lhenry, D. J. Morrissey, A. C. Veeck, and G. J. Wozniak, Phys. Rev. C **57**, 3129 (1998).

[45] F. Hubert, R. Bimbot, and H. Gauvin, At. Data Nucl. Data Tables **46**, 1 (1990).

[46] F. Hubert, R. Bimbot, and H. Gauvin, Nucl. Instrum. Methods B **36**, 357 (1989).

[47] A. Leon *et al.*, At. Data Nucl. Data Tables **69**, 217 (1998).

[48] M. Papa *et al.*, Phys. Rev. C **64**, 024612 (2001).

[49] M. Papa, T. Maruyama, and A. Bonasera, J. Comput. Phys. **208**, 403 (2005).

[50] G. A. Souliotis, J. Phys. Conf. Series **205**, 012019 (2010).

[51] F. Amorini *et al.*, Phys. Rev. Lett. **102**, 112701 (2009).

[52] J. Aichelin, Phys. Rep. **202**, 233 (1991).

[53] R. Charity *et al.*, Nucl. Phys. A **483**, 371 (1988).

[54] R. J. Charity, Phys. Rev. C **58**, 1073 (1998).

[55] K. Sümmerer and B. Blank, Phys. Rev. C **61**, 034607 (2000).

[56] P. Moller, J. R. Nix, and K. L. Kratz, At. Data Nucl. Data Tables **66**, 131 (1997).